ARTICLE

Open Access

Electrodynamics of MnBi$_2$Te$_4$ intrinsic magnetic topological insulators

Luca Tomarchio[1,2], Lorenzo Mosesso[1], Salvatore Macis[1,3], Antonio Grilli[3], Martina Romani[3], Mariangela Cestelli Guidi[3],
Kejing Zhu[4], Xiao Feng[4], Michele Zacchigna[5], Massimo Petrarca[2,6], Ke He[4] and Stefano Lupi[1,3]

Abstract
We report on the electrodynamics of MnBi$_2$Te$_4$ thin films, an intrinsic magnetic topological material. We study its optical conductivity from terahertz (THz) to ultraviolet (UV) frequencies as a function of the film thickness, highlighting the presence of surface topological states superimposed on the bulk electrodynamics response. For the thinnest film, where the charge transport is dominated by Dirac surface states, we investigate the effect of the phase transition from the high-temperature topological protected state to the low-temperature magnetic (time-reversal broken) state by measuring the optical conductivity across the Néel temperature. At low temperatures, the breaking of the time reversal symmetry affects the optical conductivity, indicating that a magnetic-induced gap opens below T_N.

Introduction

The introduction of magnetic elements into a protected topological insulator breaks the time-reversal symmetry, and the magnetic interaction can open a gap in the otherwise gapless topological Dirac surface states (DSSs)[1]. This allows various novel topological quantum states to be generated, such as magnetic topological insulators[1–3], magnetic Weyl semimetals[4,5] and axion insulators[6]. A plethora of magnetoelectric effects are predicted from the topological invariants of these novel materials, such as the quantum anomalous Hall effects (QAHE)[7–9], with the appearance of chiral dissipationless edge channels, half-quantized surface anomalous Hall conductivity[6], non-linear effects such as multiple harmonic generation[10,11] and the circular photogalvanic effect[12,13].

Doping with magnetic elements is the usual means for exploring the interaction between topology and magnetism[14]. However, doping inhomogeneity leads to complex magnetic ordering and small exchange gaps[15]. Consequently, various topological quantum effects appear at very low temperatures. Therefore, intrinsic magnetic topological insulators are highly desirable for increasing those temperatures and for investigating topological quantum phenomena.

MnBi$_2$Te$_4$ (MBT) is a novel intrinsic magnetic topological insulator where an additional layer of Mn atoms is inserted into the tetradymite structure of Bi$_2$Te$_3$, creating a septuple-layer (SL) of atoms with a Te-Bi-Te-Mn-Te-Bi-Te sequence[16,17]. The layers are then stacked through van der Waals (vdW) forces, crystallizing in a rhombohedral layered structure with the space group R-3m and creating a layered magnet similar to transition metal halides such as CrI$_3$[18–20]. In MBT, the distance between the Mn layers causes weak magnetic interlayer coupling[21], resulting in an A-type antiferromagnetic ground state with a Néel temperature of 24 K while preserving a ferromagnetic long-range order in the single SLs[22–25]. Therefore, magnetism and topology are structurally separated in MBT, with Mn layers inducing magnetism and Bi-Te layers generating topological states. This structural separation makes MBT a case study for investigating quantum topological phenomena[26–28].

The nontrivial topology results in the presence of electronic DSSs at the Γ point in the Brillouin zone, which have been observed both in single crystals[29,30] and thin

Correspondence: Stefano Lupi (stefano.lupi@uniroma1.it)
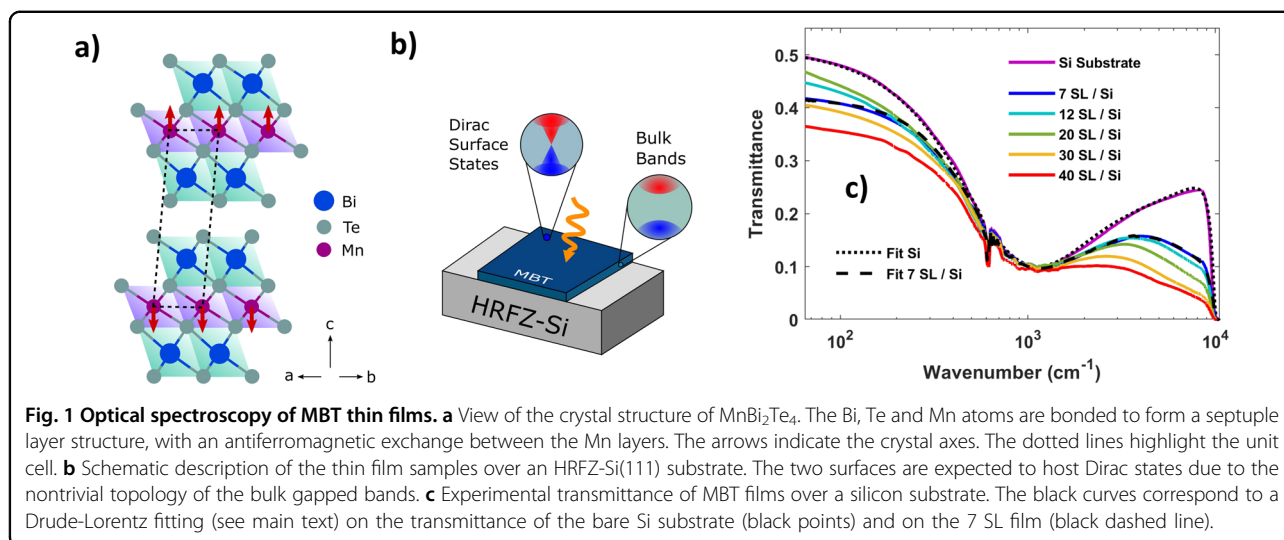[1]Department of Physics, Sapienza University, Piazzale Aldo Moro 5, 00185
Rome, Italy
[2]INFN Section of Rome, P. Le Aldo Moro, 2, 00185 Rome, Italy
Full list of author information is available at the end of the article

Fig. 1 Optical spectroscopy of MBT thin films. a View of the crystal structure of MnBi$_2$Te$_4$. The Bi, Te and Mn atoms are bonded to form a septuple layer structure, with an antiferromagnetic exchange between the Mn layers. The arrows indicate the crystal axes. The dotted lines highlight the unit cell. **b** Schematic description of the thin film samples over an HRFZ-Si(111) substrate. The two surfaces are expected to host Dirac states due to the nontrivial topology of the bulk gapped bands. **c** Experimental transmittance of MBT films over a silicon substrate. The black curves correspond to a Drude-Lorentz fitting (see main text) on the transmittance of the bare Si substrate (black points) and on the 7 SL film (black dashed line).

films[31] by angle-resolved photoemission spectroscopy (ARPES). Below the Néel temperature, the time-reversal symmetry is broken by the magnetic ordering, causing the system to enter a magnetic topological phase. In this magnetic phase, the surface Dirac states lose their protection, causing the opening of an energy gap at the Dirac point whose properties, however, are still under debate[28,32].

Although many MBT properties have already been measured in single crystals or thin flakes, it is known that topological insulator crystals can be strongly affected by impurities and stoichiometric defects[33]. Therefore, the growth of MBT thin films with well-controlled properties may remove defects and impurities, which negatively affect the single-crystal properties, to a considerable extent[11,33–36]. Indeed, nearly pure DSSs are expected at the Fermi level for thin films[31], differing from the flakes cleaved by single crystals, which have been shown to host additional electronic contributions from bulk states[29,30]. Moreover, due to the antiferromagnetic coupling between the Mn layers, the magnetic properties of MBT films can be tuned through the thin film geometry by simply changing the number of SLs, with a QAHE and an axion insulator state predicted for odd and even numbers of layers, respectively[37].
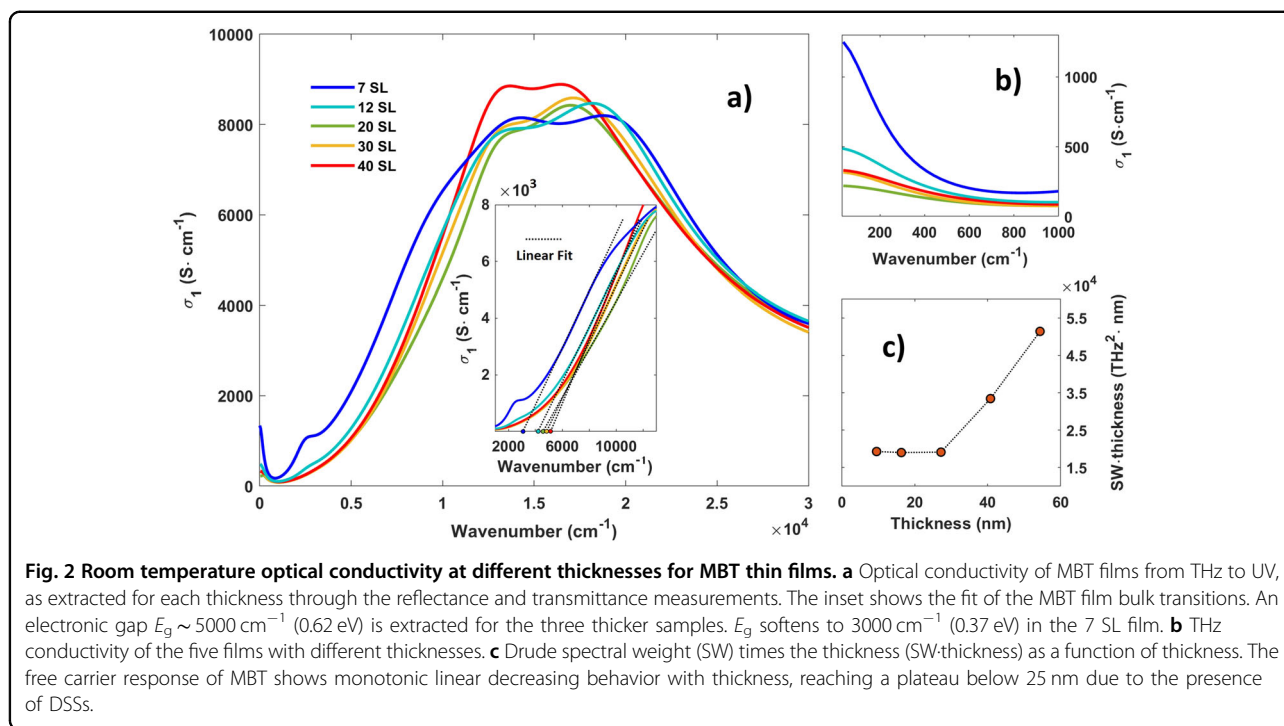
In this manuscript, we investigate the electrodynamics of high-quality MnBi2Te4 thin films deposited on high-resistivity floating-zone (HRFZ)-silicon substrates over a very broad spectral range, from terahertz (THz) to ultraviolet (UV), as a function of thickness (from 7 to 40 SLs) and temperature. The electronic response in the thinnest sample (7 SLs) is dominated by mobile Dirac surface states generating Drude behavior in the THz and infrared (IR) spectral range. Therefore, we investigate the low energy behavior of the 7 SL film at various temperatures above and below the magnetic transition (~24 K). We

observe that the broken time reversal symmetry affects the Dirac surface states at the Fermi level, opening a magnetic gap at the Dirac point of ~80 meV, in good agreement with theoretical calculations.

Results

MnBi$_2$Te$_4$ thin films were synthesized at different thicknesses through an evaporation process on an HRFZ-Si(111) substrate (see Methods). The rhombohedral crystal structure of MnBi$_2$Te$_4$ (R-3m space group) is shown in Fig. 1a. Bismuth (Bi) and tellurium (Te) atoms are bonded to form an ordered structure with a manganese (Mn) additional layer, forming a septuple layer structure, Te-Bi-Te-Mn-Te-Bi-Te and yielding intrinsic magnetic properties. The black arrows indicate the a, b, and c crystal axes, while the red arrows indicate the antiferromagnetic coupling between the Mn layers that are stacked and linked through van der Waals forces.

Reflectance (R) and transmittance (T) measurements on films at different thicknesses were performed across a broad spectral range from THz ($\simeq 30\,\text{cm}^{-1}$) to UV (30,000 cm^{-1}) frequencies. The spectroscopy setup is discussed in the Methods section and shown in Fig. 1b. Figure 1c shows the measured optical transmittance of all films and the Si substrate. Figure 2a shows the real part of the extracted optical conductivity $\sigma_1(\omega)$ of MBT films with different thicknesses across the whole measured spectrum. $\sigma_1(\omega)$ is obtained through a Kramers-Kronig constrained simultaneous fitting of reflectance and transmittance data, described through a multilayer model using the RefFIT software[38]. Examples of the transmittance fit are shown as black lines in Fig. 1c. The measured HRFZ-Si(111) optical parameters are used as inputs in the RefFIT procedure. The optical conductivity for all thicknesses is dominated by a broad absorption band located between 15,000 and 20,000 cm^{-1}, which can be associated

Fig. 2 Room temperature optical conductivity at different thicknesses for MBT thin films. a Optical conductivity of MBT films from THz to UV, as extracted for each thickness through the reflectance and transmittance measurements. The inset shows the fit of the MBT film bulk transitions. An electronic gap $E_g \sim 5000\,\mathrm{cm}^{-1}$ (0.62 eV) is extracted for the three thicker samples. E_g softens to $3000\,\mathrm{cm}^{-1}$ (0.37 eV) in the 7 SL film. **b** THz conductivity of the five films with different thicknesses. **c** Drude spectral weight (SW) times the thickness (SW·thickness) as a function of thickness. The free carrier response of MBT shows monotonic linear decreasing behavior with thickness, reaching a plateau below 25 nm due to the presence of DSSs.

with bulk interband transitions, in good agreement with data for single crystals[39]. This broad peak is well separated from a low-energy metallic contribution appearing for all films below $1000\,\mathrm{cm}^{-1}$ (see Fig. 2b).

Discussion

An estimation of the electronic gap E_g can be obtained by taking the zero crossing of a linear fitting curve for the interband conductivity onset. This fitting is plotted for all films in the inset of Fig. 2a through dashed black lines. Their intersections with the frequency axis provide an estimation for the energy gap. E_g is on the order of $5000\,\mathrm{cm}^{-1}$ (0.62 eV) for the three (20, 30 and 40 SL) thicker films. The gap is subjected to a redshift with decreasing thickness, reaching nearly $3000\,\mathrm{cm}^{-1}$ (0.37 eV) in the 7 SL film. Although the gap values estimated from our optical measurements are higher than the absorption edge obtained from bulk MBT[22,29,39,40] (nearly 200 meV), they are in good agreement with ARPES studies on the same films[31]. Moreover, near $2500\,\mathrm{cm}^{-1}$ (0.3 eV), an additional absorption feature appears for the 7 and 12 SL films at variance with the results of the thicker films, which instead exhibit a smooth decreasing behavior. Given its energy range, this extra peak could be associated with transitions from the lower energy Dirac cone to the upper one, analogous to the Pauli blocking transitions in graphene.

Figure 2b shows the real part of the optical conductivity in the terahertz spectral range, highlighting the metallic absorption edge coming from the low energy states. Strong thickness-dependent changes can be observed, with the

thinner 7 SL sample exhibiting a conductivity almost 4 times higher than that of the 40 SL film. To highlight the contribution of the surface states to the low-energy electrodynamics of MBT, we fit the low-energy optical conductivity with a Drude term characterized by a scattering rate Γ and a spectral weight $SW = \omega_p^2/8$, where ω_p is the plasma frequency. To understand the surface contributions to the Drude response, the spectral weight is multiplied by the thickness d of the films. This result is plotted in Fig. 2c as a function of d. Here, the metallic contribution is nearly constant for the 7, 12 and 20 SL films and grows in a roughly linear way at larger thicknesses. The nearly constant value of $SW \times d$ for films between 7 and 20 SLs suggests that in those films, the free-charge contribution mainly comes from Dirac surface states. This result also supports a surface-related origin for the E_g redshift and the increase in strength of the oscillator near $2500\,\mathrm{cm}^{-1}$ (see Fig. 2a), both found in the thinner films, where the topological surface states are expected to contribute strongly to the optical conductivity.

Supposing the conductivity of the 7 SL film fully originates from the 2D surface states, it is possible to link its Drude spectral weight to the density of carriers n_{2D} as[41]

$$\omega_p^2 d = \frac{n_{2D}e^2}{m^* \epsilon_0} \tag{1}$$

where m^* is the mass for the Dirac fermions of the surface states, obtained as the ratio of the Fermi momentum k_F and velocity v_F: $m^* = \hbar k_F / v_F$. Considering the surface state
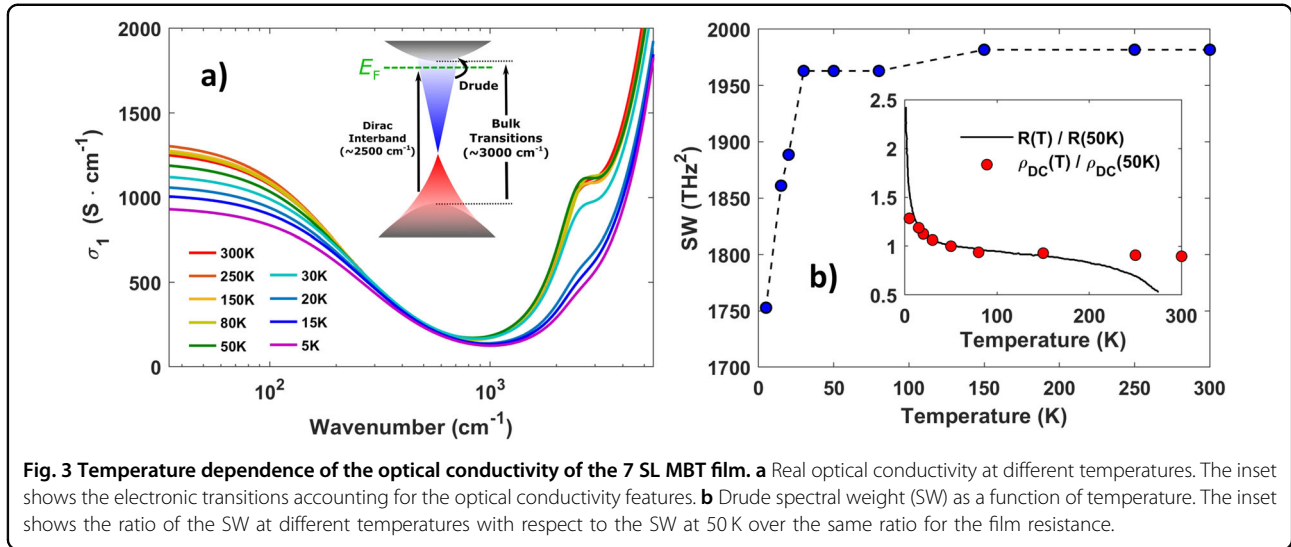
Fig. 3 Temperature dependence of the optical conductivity of the 7 SL MBT film. a Real optical conductivity at different temperatures. The inset shows the electronic transitions accounting for the optical conductivity features. **b** Drude spectral weight (SW) as a function of temperature. The inset shows the ratio of the SW at different temperatures with respect to the SW at 50 K over the same ratio for the film resistance.

dispersion as purely linear near the Fermi level[31], the right part of Eq. (1) can be written as[41]

$$\omega_p^2 d = \frac{G_0}{\hbar} \frac{E_F}{\epsilon_0} \qquad (2)$$

where G_0 is the quantum of conductance ($G_0 = 2e^2/h \simeq 7.75 \times 10^{-5}$ S) and $E_F = \hbar k_F \nu_F$ is the Fermi energy. From the Drude fitting, we can thus determine $E_F \sim 120\ meV$, and using the constant Fermi velocity $\nu_F = \nu_F = 5.5 \times 10^5$ m/s extracted by ARPES measurements[31], a Fermi wavevector $k_F \sim 0.04\,\text{Å}^{-1}$ is estimated, which can be compared to the result $k_F \sim 0.07\,\text{Å}^{-1}$ obtained by ARPES[31].

Temperature-dependent optical conductivity

As shown in the previous section, the optical conductivity of the 7 SL thin film is dominated by Dirac surface states. Therefore, we investigate its optical behavior as a function of temperature to study the effect of the magnetic order and then of the time-reversal breaking on the Dirac surface states. In this regard, optical transmittance measurements were performed between 20 and 10,000 cm^{-1} from 300 K to 5 K, crossing the Néel temperature at ~24 K. The real part of the optical conductivity is shown in Fig. 3a, as extracted from transmittance measurements through the RefFit program. The optical conductivity from 300 to 50 K (above the Néel temperature) is nearly constant, showing a Drude term (associated with mobile Dirac surface states) below 1000 cm^{-1}, an absorption band in the mid-infrared (MIR) at ~2500 cm^{-1} (310 meV) and, at higher frequency, the absorption tail related to interband bulk transitions, whose linear extrapolation to the frequency axis provides an electronic gap of ~3000 cm^{-1} (see above). The inset in Fig. 3a schematically describes these electronic transitions. Below $T_N \simeq 24$ K, the optical conductivity decreases

over the whole spectral range with respect to that at all other temperatures. More specifically, the electronic gap hardens to ~4000 cm^{-1}, the Drude term is reduced in intensity, and the MIR absorption band nearly disappears. This is at variance with single-crystal measurements, where an increase in the optical conductivity with decreasing temperature is observed, as given by the reduced scattering of the bulk electrons[22,39].

The effect of magnetism on the DSSs can be quantified by plotting the Drude spectral weight *SW* as a function of temperature (see Fig. 3b). Here, the *SW* is approximately constant above 30 K, while it decreases rapidly without disappearing down to 5 K, i.e., well below the Néel temperature. Our optical conductivity measurements reproduce the DC behavior of the resistance *R* on a film of the same batch well, as shown in the inset of Fig. 3b. Here, we plot the ratio $R(T)/R(50K)$ vs. *T* (black line) in comparison to the zero-frequency extrapolation of the optical resistivity ($\rho_{DC} = 1/\sigma_1(\omega = 0)$) normalized at 50 K ($\rho_{DC}(T)/\rho_{DC}(50\,\text{K})$). In addition to some discrepancies observed at approximately room temperature (probably caused by an extra temperature dependence of the silicon substrate), the two ratios behave in a very similar way, indicating that the increase of the resistance below the Néel temperature can be linked to the reduction of the Drude spectral weight as induced by the breaking of the time-reversal symmetry. Indeed, broken time-reversal symmetry is expected to remove the topological protection of DSSs[2], inducing the formation of a gap at the Dirac node. In this framework, the gap opening modifies the linear (Dirac) energy-momentum dispersion which, in the magnetic phase, should become $E(k) = \pm \sqrt{\hbar^2 \nu_F^2 k^2 + \Delta^2}$, where 2Δ is the gap value[2]. Since in MBT the Dirac node is located well below the Fermi level ($\simeq -0.12$ eV), the gap opening should only partially affect

the electronic transitions near the Fermi level, such as the Drude term, whose spectral weight is dampened due to the modified energy-momentum dispersion. In other words, the gap opening corresponds to the Dirac quasiparticles acquiring an effective mass, thus decreasing their mobility and conductivity contribution. An estimate of the gap value can be obtained from the Drude SW reduction below T_N, again using Eq. (1), as explained in the methods section. From this calculation, a gap value $2\Delta \simeq 80$ meV is extracted. Our results are at variance with recent high-resolution ARPES data on single crystals[29], highlighting an unperturbed Dirac node even below T_N. However, they are in good agreement with recent ARPES results obtained on MBT thin films grown via MBE[42], which evidence a large energy gap (>70 meV) below the Néel temperature for a 5 SL film on silicon. This result confirms the importance of thin film geometry in highlighting the magnetic gap opening and as a platform where topological surface states, overcoming bulk contribution, can be used for device applications. Moreover, our results are in good agreement with theoretical calculations[28] and point contact tunneling spectroscopy results[43]. These results suggest a magnetic gap of ~50–60 meV (~400–500 cm^{-1}), slightly lower than the value extracted in this work, $2\Delta \simeq 80$ meV. Therefore, the evidence of a gap opening below T_N, along with the dominant surface state behavior at the Fermi level, highlights the intrinsic topological character of MBT thin films, in stark contrast with single crystals and thin flakes.

Conclusions

In this work, we investigated the optical properties of intrinsic magnetic topological $MnBi_2Te_4$ material over a broad spectral range from terahertz to ultraviolet. High-quality MBT thin films were studied at room temperature with different thicknesses, from 7 to 40 septuple layers, allowing us to separate the contribution of Dirac surface free-electron states in the optical conductivity from bulk electronic transitions. In the 7 SLs (where the Dirac surface states provide the major contribution to the low-energy conductivity), we further studied the behavior of these states crossing the Néel critical temperature at nearly 24 K and entering the magnetically time-reversal broken state. The temperature-dependent optical conductivity measurements indicate the opening of a gap at the Dirac node, as induced by the broken time-reversal symmetry, in stark contrast to ARPES measurements in both single crystals and thin flakes, where contradictory results have been obtained. From the reduction of the Drude spectral weight below T_N, we estimated a gap on the order of 80 meV, which is in good agreement with calculation and tunneling measurements. This optical study indicates that an intrinsic topological behavior is observed in $MnBi_2Te_4$ thin films, paving the road for exploring the interaction between magnetism and

topology and the appearance of novel electrodynamics effects[31,40,44,45].

Methods
Thin film growth

The Si(111) substrates (resistivity 10000 Ohm cm) were cleaned by flashing to 1200 °C in an ultrahigh vacuum chamber for MBE growth (base pressure 10^{-9} mbar). The treated Si(111) substrates showed sharp 7 × 7 reconstruction patterns from reflection high energy election diffraction. High purity Bi (99.9999%), Mn (99.9999%) and Te (99.9999%) were coevaporated onto the substrates, which were kept at a certain temperature of 230 °C. The growth was carried out under Te-rich conditions, and the flux ratio between Mn and Bi was kept at nominally 1:2. The growth rate was 1 SL/7 min. Postannealing at 250 °C was carried out to improve the crystalline quality[46].

Optical characterization

Transmission and reflection measurements were taken through a Vertex 70 v FTIR broadband interferometer coupled with different detection systems to scan the spectral range from THz (20 cm^{-1}) to NIR (10,000 cm^{-1}). Reflectivity measurements were collected at higher frequencies up to ultraviolet wavelengths (30,000 cm^{-1}) by a JASCO V770 spectrometer. The MBT thin films were measured at various temperatures through a He-cooled Helitran cryostat. The optical properties of the Si substrate were measured under the same experimental conditions, and the real (n) and imaginary (k) parts of the refraction index were determined by the Refit program. n and k were used as input parameters in a film/substrate bilayer model[38] to extract the real and imaginary parts of the film optical conductivity.

The transport data of the 7 SL $MnBi_2Te_4$ film were measured from a film grown under the same growth conditions as the sample used for the optical conductivity measurements. The low-temperature transport measurements were taken in a closed-cycle system (Oxford Instruments TelatronPT). Freshly cut indium cubes were cold pressed onto the sample as contacts. Standard lock-in techniques were employed to determine the sample resistance in a four-terminal configuration.

Calculation of the gap at the dirac node

Using Eq. (1), the ratio between the SW of the film at two different temperatures, T_1 and T_2, can be linked with the change in the effective mass m^* and the 2D surface electron density n_{2D} as follows:

$$\frac{SW_{T_1}}{SW_{T_2}} = \frac{m^*_{T_2}}{m^*_{T_1}} \frac{n_{2D,T_1}}{n_{2D,T_2}} \qquad (3)$$

To understand the effect of the magnetic phase transition on the spectral weight, we choose the experimental

temperatures $T_1 = T_> > T_N$ and $T_2 = T_< < T_N$, respectively, above and below the Néel temperature T_N. The 2D electron density for a single surface takes the form $n_{2D} = k_F^2/4\pi41$, while the effective mass is $m^* = \hbar k_F/v_F$, where $v_F = (1/\hbar)\partial E_F/\partial k_F$ is the Fermi velocity. By using the gapped energy-momentum dispersion $E_F = \sqrt{(\hbar v_F k_F)^2 + \Delta^2}$ for $T_<$, where 2Δ is the gap[2], Eq. (3) can be written as

$$\frac{SW_{T_>}}{SW_{T_<}} = \sqrt{\frac{E_F^2 + \Delta^2}{E_F^2 - \Delta^2}} \tag{4}$$

which describes a reduction of the Drude spectral weight in the magnetic ordered state, quantified by the gap value. Using the experimental data, i.e., $T_< = 5\,\text{K}$, $T_> = 50\,\text{K}$, and E_F, as obtained by Eq. (2) (the Fermi energy is approximately constant across the transition), a gap value of $2\Delta \simeq 80\,meV$ is obtained.

Author details
[1]Department of Physics, Sapienza University, Piazzale Aldo Moro 5, 00185 Rome, Italy. [2]INFN Section of Rome, P. Le Aldo Moro, 2, 00185 Rome, Italy. [3]INFN—Laboratori Nazionali di Frascati, via Enrico Fermi 54, 00044 Frascati (Rome), Italy. [4]State Key Laboratory of Low Dimensional Quantum Physics, Department of Physics, Tsinghua University, and Beijing Academy of Quantum Information Sciences, Beijing 100193, China. [5]CNR-IOM, S.S. 14 Km 163.5 in Area Science Park, 34149 Basovizza - Trieste, Italy. [6]SBAI Department, Sapienza University, Piazzale Aldo Moro 5, 00185 Rome, Italy

Author contributions
All authors contributed extensively to the work presented in this paper. L.T., L.M., and S.L. designed the experiment. S.L. and K.H. supervised the work. K.Z. and X.F. prepared the samples. L.T., A. G., M. C. G, L. M., M. R., M.Z., and S.M. measured the optical transmittance and reflectance. L.T. and L.M. analyzed the data. L.T., L.M., and S.L. prepared the original draft. All authors reviewed and edited the manuscript. All authors have read and agreed to the published version of the manuscript.

Competing interests
The authors declare no competing interests.

Publisher's note
Springer Nature remains neutral with regard to jurisdictional claims in published maps and institutional affiliations.

References
1. Hasan, M. Z. & Kane, C. L. Colloquium: Topological insulators. *Rev. Mod. Phys.* **82**, 3045 (2010).
2. Tokura, Y., Yasuda, K. & Tsukazaki, A. Magnetic topological insulators. *Nat. Rev. Phys.* **1**, 126–143 (2019).
3. Ortmann, F., Roche, S. & Valenzuela, S. O. Topological Insulators: Fundamentals and Perspectives. Wiley-VCH Verlag GmbH & Co. KGaA, Boschstr. 12, 69469 Weinheim, Germany (2015).
4. Araki, Y. Magnetic textures and dynamics in magnetic weyl semimetals. *Ann. Phys.* **532**, 1900287 (2019).
5. Destraz, D. et al. Magnetism and anomalous transport in the Weyl semimetal PrAlGe: possible route to axial gauge fields. *npj Quantum Mater.* **5**, 5 (2020).
6. Mong, R. S. K., Essin, A. M. & Moore, J. E. Antiferromagnetic topological insulators. *Phys. Rev. B* **81**, 245209 (2010).
7. Nagaosa, N., Sinova, J., Onoda, S., MacDonald, A. H. & Ong, N. P. Anomalous Hall effect. *Rev. Mod. Phys.* **82**, 1539 (2010).
8. Chang, C.-Z. et al. Experimental observation of the quantum anomalous Hall effect in a magnetic topological insulator. *Science* **340**, 167–170 (2013).
9. Liu, E. et al. Giant anomalous Hall effect in a ferromagnetic kagome-lattice semimetal. *Nat. Phys.* **14**, 1125–1131 (2018).
10. Morimoto, T. & Nagaosa, N. Topological nature of nonlinear optical effects in solids. *Sci. Adv.* **2**, e1501524 (2016).
11. Giorgianni, F. et al. Strong nonlinear terahertz response induced by Dirac surface states in Bi_2Se_3 topological insulator. *Nat. Commun.* **7**, 11421 (2016).
12. Chan, C.-K., Lindner, N. H., Refael, G. & Lee, P. A. Photocurrents in Weyl semimetals. *Phys. Rev. B* **95**, 041104 (2017).
13. De Juan, F., Grushin, A. G., Morimoto, T. & Moore, J. E. Quantized circular photogalvanic effect in Weyl semimetals. *Nat. Commun.* **8**, 15995 (2017).
14. Teng, J., Liu, N. & Li, Y. Mn-doped topological insulators: a review. *J. Semicond.* **40**, 081507 (2019).
15. Hesjedal, T. Rare earth doping of topological insulators: a brief review of thin film and heterostructure systems. *Phys. Status Solidi A* **216**, 1800726 (2019).
16. Yan, J.-Q. et al. Crystal growth and magnetic structure of $MnBi_2Te_4$. *Phys. Rev. Mater.* **3**, 064202 (2019).
17. Ding, L. et al. Crystal and magnetic structures of magnetic topological insulators $MnBi_2Te_4$ and $MnBi_4Te_7$. *Phys. Rev. B* **101**, 020412 (2020).
18. Dillon, J. F. Jr., Kamimura, H. & Remeika, J. P. Magneto-optical properties of ferromagnetic chromium trihalides. *J. Phys. Chem. Solid* **27**, 1531–1549 (1966).
19. Liu, Y. et al. Thickness-dependent magnetic order in CrI_3 single crystals. *Sci. Rep.* **9**, 13599 (2019).
20. Tomarchio, L. et al. Low energy electrodynamics of CrI_3-layered ferromagnet. *Sci. Rep.* **11**, 23405 (2021).
21. Hu, C. et al. A van der Waals antiferromagnetic topological insulator with weak interlayer magnetic coupling. *Nat. Commun.* **11**, 97 (2020).
22. Estyunin, D. A. et al. Signatures of temperature driven antiferromagnetic transition in the electronic structure of topological insulator $MnBi_2Te_4$. *APL Mater.* **8**, 021105 (2020).
23. Li, H. et al. Antiferromagnetic topological insulator $MnBi_2Te_4$: synthesis and magnetic properties. *Phys. Chem. Chem. Phys.* **22**, 556–563 (2020).
24. Li, B. et al. Competing magnetic interactions in the antiferromagnetic topological insulator $MnBi_2Te_4$. *Phys. Rev. Lett.* **124**, 167204 (2020).
25. Deng, Y. et al. Quantum anomalous Hall effect in intrinsic magnetic topological insulator $MnBi_2Te_4$. *Science 367*, **6480**, 895–900 (2020).
26. Li, J. et al. Intrinsic magnetic topological insulators in van der Waals layered $MnBi_2Te_4$ family materials. *Sci. Adv.* **5**, 6 (2019).
27. He, K. $MnBi_2Te_4$ family intrinsic magnetic topological materials. *npj Quantum Mater.* **5**, 90 (2020).
28. Zhang, D. et al. Topological axion states in the magnetic insulator $MnBi_2Te_4$ with the quantized magnetoelectric effect. *Phys. Rev. Lett.* **122**, 206401 (2019).
29. Hao, Y.-J. et al. Gapless surface dirac cone in antiferromagnetic topological insulator $MnBi_2Te_4$. *Phys. Rev. X* **9**, 041038 (2019).
30. Vidal, R. C. et al. Surface states and Rashba-type spin polarization in antiferromagnetic $MnBi_2Te_4$(0001). *Phys. Rev. B* **100**, 121104 (2019).
31. Gong, Y. et al. Experimental realization of an intrinsic magnetic topological insulator. *Chin. Phys. Lett.* **36**, 7 (2019).
32. Liu, C. et al. Robust axion insulator and Chern insulator phases in a two-dimensional antiferromagnetic topological insulator. *Nat. Mater.* **19**, 522–527 (2020).
33. Di Pietro, P. et al. Optical conductivity of bismuth-based topological insulators. *Phys. Rev. B* **86**, 045439 (2012).

34. Di Pietro, P. et al. Observation of Dirac plasmons in a topological insulator. *Nat. Nanotechnol.* **8**, 556 (2013).

35. Autore, M. et al. Topologically protected Dirac plasmons and their evolution across the quantum phase transition in a $(Bi_{1-x}In_x)_2Se_3$ topological insulator. *Nanoscale* **8**, 4667 (2016).

36. Autore, M. et al. Plasmon–phonon interactions in topological insulator microrings. *Adv. Optical Mater.* **3**, 1257 (2015).

37. Shikin, A. M. et al. Nature of the Dirac gap modulation and surface magnetic interaction in axion antiferromagnetic topological insulator $MnBi_2Te_4$. *Sci. Rep.* **10**, 13226 (2020).

38. Kuzmenko, A. B. Kramers-Kronig constrained variational analysis of optical data. *Rev. Sci. Instrum.* **76**, 083108 (2005).

39. Köpf, M., Ebad-Allah, J., Lee, S. H., Mao, Z. Q. & Kuntscher, C. A. Influence of magnetic ordering on the optical response of the antiferromagnetic topological insulator $MnBi_2Te_4$. *Phys. Rev. B* **102**, 165139 (2020).

40. Chen, B. et al. Intrinsic magnetic topological insulator phases in the Sb doped $MnBi_2Te_4$ bulks and thin flakes. *Nat. Commun.* **10**, 4469 (2019).

41. Wu, L. et al. High-resolution Faraday rotation and electron-phonon coupling in surface states of the bulk-insulating topological insulator $Cu_{0.02}Bi_2Se_3$. *Phys. Rev. Lett* **115**, 217602 (2015).

42. Trang, C. X. et al. Crossover from 2D ferromagnetic insulator to wide band gap quantum anomalous hall insulator in ultrathin $MnBi_2Te_4$. *ACS Nano* **15**, 13444–13452 (2021).

43. Ji, H.-R. et al. Detection of magnetic gap in topological surface states of $MnBi_2Te_4$. *Chin. Phys. Lett.* **38**, 10 (2021).

44. Xu, L. et al. Persistent surface states with diminishing gap in $MnBi_2Te_4/Bi_2Te_3$ superlattice antiferromagnetic topological insulator. *Sci. Bull.* **65**, 2086–2093 (2020).

45. Klimovskikh, I. I. et al. Tunable 3D/2D magnetism in the $(MnBi_2Te_4)(Bi_2Te_3)_m$ topological insulators family. *npj Quantum Mater.* **5**, 54 (2020).

46. Zhu, K. et al. Investigating and manipulating the molecular beam epitaxy growth kinetics of intrinsic magnetic topological insulator $MnBi_2Te_4$ with in situ angle-resolved photoemission spectroscopy. *J. Phys: Condens. Matter* **32**, 475002 (2020).